Crystalline nodal topological superconductivity in monolayer NbSe$_2$

Daniel Shaffer,[1] Jian Kang,[2] F. J. Burnell,[1] and Rafael M. Fernandes[1]

[1]*School of Physics and Astronomy, University of Minnesota, Minneapolis, Minnesota 55455, USA*
[2]*National High Magnetic Field Laboratory, Florida State University, Tallahassee, Florida 32310, USA*
(Dated: April 12, 2019)

We present a microscopic calculation of the phase diagram of the Ising superconductor NbSe$_2$ in the presence of both in-plane magnetic fields and Rashba spin-orbit coupling. Repulsive interactions lead to two distinct instabilities, in singlet- and triplet- interaction channels. In the regime of large fields, the topological character of the superconducting state depends strongly on the magnetic field direction. When the field is applied along one of the three Γ-K lines, a crystalline nodal topological superconducting phase is stabilized, whereas for other field directions the pairing state is topologically trivial. In the regime of large Rashba and dominant triplet interactions, a chiral topological superconducting phase emerges, in which time-reversal symmetry is spontaneously broken and the system acquires a Chern number of ± 6.

Introduction. The observation of superconductivity (SC) in 1H monolayer transition metal dichalcogenides such as NbSe$_2$ and MoS$_2$ opens a new avenue to explore superconductivity in systems with strongly coupled spin-orbital degrees of freedom [1–11]. In contrast to their bulk counterparts, in-plane inversion symmetry is broken in these monolayers, giving rise to an *Ising* spin-orbit coupling (SOC) that forces the spins to point out-of-plane [7, 8, 12–14]. This Ising SOC is believed to be responsible for the experimental observation that the superconducting state survives up to remarkably large in-plane magnetic fields, far beyond the usual Pauli limit [5–7, 10, 15, 16].

The combination of large Ising SOC, which lifts the spin degeneracy, together with multiple Fermi pockets, has inspired considerable interest in the potential for unconventional superconductivity in these materials [12, 15, 17–27]. In gated MoS$_2$, which has four spin-split Fermi pockets centered at the $\pm K$ points of the hexagonal Brillouin zone, repulsive inter-band interactions can stabilize a fully gapped triplet SC state [19, 24, 25]. Chiral topological superconductivity [28] both with and without large Rashba SOC has also been predicted in MoS$_2$ [24, 26, 29], as has finite-momentum Cooper pairing [26]. In NbSe$_2$ and its close relative TaS$_2$, which have Fermi pockets centered at the $\pm K$ and Γ points, it was argued that for in-plane magnetic fields larger than the Pauli limiting field, a nodal topological SC state is realized, protected by an anti-unitary time-reversal like symmetry and characterized by Majorana flat bands at the sample's edges [17, 22].

Despite the flurry of activity on this front, important questions about these SC states remain unaddressed, particularly regarding their microscopic origin and their stability in realistic experimental conditions. Elucidating these issues is essential not only from a fundamental standpoint, but also to provide concrete guidance for experiments. In this paper, we present a microscopic theory of superconductivity in NbSe$_2$. Our focus is on determining the phase diagram as a function of two experimentally tunable quantities: Rashba SOC, with energy scale $\alpha_R p_F$ (p_F is the Fermi momentum), which can be con-
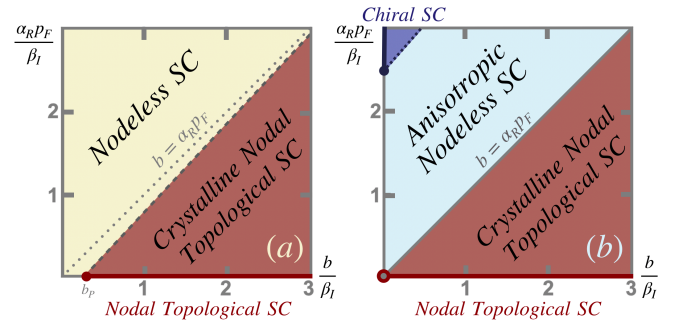

FIG. 1. Phase diagram for NbSe$_2$ as a function of the Rashba SOC (α_R) and in-plane magnetic field **B** oriented along the Γ-K direction, in units of the Ising SOC β_I. In panel (a) (panel (b)), the leading SC instability for $\alpha_R = B = 0$ is a singlet extended s-wave state (triplet f-wave state). Dots and solid lines denote phase transition boundaries; dashed lines indicate approximate boundaries.

trolled by gating or by the choice of substrate, and an in-plane magnetic field **B**. Whereas the effects of Ising SOC, $\alpha_R p_F$ and **B** on different superconducting states have been studied separately [15, 17, 20–22, 30–32], their combined role has yet to be addressed. Moreover, in contrast to several previous investigations, here the possible SC states are microscopically determined from the repulsive electronic interactions that are allowed by the fermiology of NbSe$_2$.

Our analysis reveals two distinct (B, α_R) phase diagrams, shown in Fig. 1. If the inter-band repulsion coupling the Γ and $\pm K$ Fermi pockets dominates, the SC state for $B = \alpha_R = 0$ is a singlet extended s-wave state with nearly isotropic gaps of opposite signs at Γ and $\pm K$ (Fig. 1a). If the inter-band processes coupling the K and $-K$ Fermi pockets dominates, the SC instability for $B = \alpha_R = 0$ is towards a triplet f-wave state, characterized by isotropic gaps of opposite signs at K and $-K$, and a nodal gap at Γ.

These two phase diagrams host two topological superconducting phases distinct from those previously discussed for NbSe$_2$. First, we find that the nodal topologi-
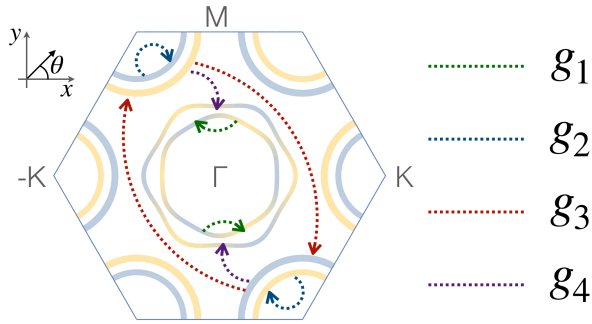
FIG. 2. The Fermi surface of NbSe$_2$ in the presence of Ising SOC and a weak Rashba SOC. The colors indicate the out-of-plane spin polarization of each pocket. The arrows denote the four distinct types of repulsive electronic interactions that contribute to the pairing instability.

cal phase predicted at magnetic fields exceeding the Pauli limit in [17] is destroyed by an arbitrarily small Rashba SOC, which lifts the nodes as it breaks the time-reversal-like symmetry that protects them. However, when the **B** field is parallel to one of the Γ-K directions, the system realizes a *crystalline* nodal topological SC, with zero-energy boundary flat bands protected by a mirror symmetry. Second, when inter-band repulsion between the K and $-K$ pockets dominates over inter-band repulsion between K and Γ pockets, for $B \simeq 0$ but large α_R we find a chiral topological $p \pm ip$ SC that spontaneously breaks time-reversal symmetry, with a thermal Hall conductance $\kappa_{xy} = 6 \left(\pi^2 k_B^2 / 3h \right) T$.

Microscopic model and superconductivity. The Fermi surface of undoped NbSe$_2$ is shown in Fig. 2. The non-interacting Hamiltonian is given by:

$$H_0 = \sum_{\eta \mathbf{p}} \psi_{\eta, \mathbf{p}}^\dagger \left[\epsilon_\eta(\mathbf{p}) + \beta_\eta(\mathbf{p}) \sigma^z + \alpha_R (\boldsymbol{\sigma} \times \mathbf{p})_z \right] \psi_{\eta, \mathbf{p}} \quad (1)$$

where $\psi_{\eta, \mathbf{p}}^\dagger = (d_{\eta, \mathbf{p}\uparrow}^\dagger, d_{\eta, \mathbf{p}\downarrow}^\dagger)$ and $d_{\eta, \mathbf{p}s}^\dagger$ creates an electron at band η with spin $s = \uparrow, \downarrow$ and momentum $\mathbf{p}$ measured relative to the center of the pocket. The Fermi surface has three pairs of spin-split hole pockets centered at the $\eta = \pm K, \Gamma$ points of the Brillouin zone. Here $\epsilon_\eta(\mathbf{p}) = -\frac{p^2}{2m_\eta} - \mu$ is the band dispersion, with band masses m_η satisfying $m_K = m_{-K}$. The Ising SOC has the form $\beta_{\pm K} = \pm \beta_I$ near the $\pm K$ points and $\beta_\Gamma = 2\lambda p^3 \cos 3\theta$ near the Γ point, where θ is the angle measured relative to the Γ-K direction (see Fig. 2). Although Ising SOC vanishes along the Γ-M lines, α_R does not, so the spin-degeneracy is fully lifted on all Fermi pockets. An in-plane magnetic field **B** adds a term $H_{\text{Zeeman}} = -\sum_{\eta \mathbf{p}} \psi_{\eta, \mathbf{p}}^\dagger (\mathbf{b} \cdot \boldsymbol{\sigma}) \psi_{\eta, \mathbf{p}}$, where $\mathbf{b} \equiv g_L \mu_B \mathbf{B}$ and g_L is the Landé g-factor; this also lifts the spin-degeneracy along the Γ-M lines.

There are eight possible momentum-independent electronic interactions g_i corresponding to density-density, pair-hopping, and exchange-like processes involving the low-energy states (see e.g. [26, 33]). The absence of

nesting in the Fermi surface ensures that the only instability driven by these low-energy states is the SC one. Of the eight interactions, only the four shown in Fig. 2 contribute directly to such pairing: intra-pocket density-density interactions involving the Γ (g_1) and the $\pm K$ (g_2) pockets; and inter-pocket pair-hopping interactions between K and $-K$ (g_3) and between Γ and $\pm K$ (g_4). The interacting Hamiltonian relevant to superconductivity is thus given by (momentum indices are suppressed for simplicity):

$$H_{\text{Int}} = \frac{g_1}{2} d_{\Gamma s}^\dagger d_{\Gamma s'}^\dagger d_{\Gamma s} d_{\Gamma s'} + \frac{g_2}{2} d_{Ks}^\dagger d_{-Ks'}^\dagger d_{Ks} d_{-Ks'} +$$
$$+ \frac{g_3}{2} d_{Ks}^\dagger d_{-Ks'}^\dagger d_{-Ks} d_{Ks'} + \frac{g_4}{2} d_{\pm Ks}^\dagger d_{\mp Ks'}^\dagger d_{\Gamma s'} d_{\Gamma s} + \text{h.c.}$$
$$(2)$$

To analyze the SC instabilities in the absence of SOC and magnetic fields, we introduce the gap functions at the Γ pocket, $(\Delta_\Gamma(\mathbf{p}))_{ss'} \propto \langle d_{\Gamma, \mathbf{p}s} d_{\Gamma, -\mathbf{p}s'} \rangle$, and at the $\pm K$ pockets, $(\Delta_K(\mathbf{p}))_{ss'}^{\varepsilon \varepsilon'} \propto \langle d_{\varepsilon K, \mathbf{p}s} d_{\varepsilon' K, -\mathbf{p}s'} \rangle$, and solve the linearized gap equations (see supplementary material, SM). Here s, s' are spin indices and $\varepsilon, \varepsilon' = \pm 1$ are valley indices. Focusing on pairing with zero center-of-mass momentum forces ε and ε' to be opposite. Even when all g_i interactions are purely repulsive, there are two possible SC instabilities, provided that one of the inter-pocket interactions, g_3 or g_4, overcomes the intra-pocket repulsion promoted by g_1 and g_2. When g_4 is dominant, the resulting SC state is a singlet s-wave, with isotropic gaps $(\Delta_\Gamma(\mathbf{p}))_{ss'} = \Delta_{\Gamma,0} (i\sigma_y)_{ss'}$ and $(\Delta_K(\mathbf{p}))_{ss'}^{\varepsilon \varepsilon'} = \Delta_{K,0} (i\sigma_y)_{ss'} (\tau_x)_{\varepsilon \varepsilon'}$. Here, $\boldsymbol{\sigma}$ and $\boldsymbol{\tau}$ are Pauli matrices in spin and valley spaces, respectively. Because the two gaps have opposite signs, $\text{sgn}(\Delta_{\Gamma,0}) = -\text{sgn}(\Delta_{K,0})$, this is the so-called extended s-wave or $s^\pm$-wave state, previously proposed to be realized e.g. in iron pnictides [34] and strontium titanate [35].

In contrast, when g_3 is the dominant interaction, the SC instability is towards a triplet f-wave state, characterized by $(\Delta_\Gamma(\mathbf{p}))_{ss'} = [(\mathbf{d}_\Gamma(\mathbf{p}) \cdot \boldsymbol{\sigma}) i\sigma_y]_{ss'}$ and $(\Delta_K(\mathbf{p}))_{ss'}^{\varepsilon \varepsilon'} = [(\mathbf{d}_K(\mathbf{p}) \cdot \boldsymbol{\sigma}) i\sigma_y]_{ss'} (i\tau_y)_{\varepsilon \varepsilon'}$. Here, $\mathbf{d}_\Gamma(\mathbf{p}) = \Delta_{\Gamma,0} \cos 3\theta \, \hat{\mathbf{d}}_\Gamma$ is the d-vector of the Γ pocket gap, whereas $\mathbf{d}_K(\mathbf{p}) = \Delta_{K,0} \hat{\mathbf{d}}_K$ is the d-vector of the K pocket gap. Unlike typical triplet gaps, here $\mathbf{d}_K(\mathbf{p})$ is momentum independent, as $\Delta_K(\mathbf{p})$ is anti-symmetric in the valley degrees of freedom. Note that if we only used the momentum-independent interactions in Eq. (S1), $\Delta_\Gamma(\mathbf{p})$ would formally be zero. We therefore include sub-leading momentum-dependent interactions, which do not contribute significantly to the pairing instability, such that $\Delta_\Gamma(\mathbf{p})$ becomes non-zero (see SM).

While here our focus is on SC due to purely electronic interactions, the SC states obtained above are not necessarily inconsistent with attractive electron-phonon interactions. This is particularly the case if their main effect is to promote intra-pocket attraction, which would reduce the amplitude – or even change the sign – of the g_1, g_2

terms. On the other hand, if they have a strong effect on the inter-pocket terms, a standard s-wave SC state may be favored instead.

Superconducting phase diagrams in the presence of SOC. To solve the gap equations in the presence of Ising and Rashba SOC, as well as magnetic fields, we first perform a unitary transformation $U_{\eta\tau}^s(\mathbf{p})$ that diagonalizes the non-interacting Hamiltonian $H_0 + H_{\text{Zeeman}}$, resulting in new electronic operators $c_{\eta,\mathbf{p}\tau} = U_{\eta\tau}^s(\mathbf{p}) d_{\eta,\mathbf{p}s}$. Here, $\tau = \pm 1$ replaces the spin index $s = \uparrow, \downarrow$ and labels respectively the inner and outer non-spin-degenerate pockets centered at $\eta = \Gamma, \pm K$. The out-of-plane spin components on each pocket are illustrated in Fig. 2. For SC states with zero momentum, the paired electrons are either both from inner pockets or both from outer pockets. The gap functions are now $\Delta_{\eta\tau}(\mathbf{p}) \propto \langle c_{\eta\mathbf{p}\tau} c_{-\eta-\mathbf{p}\tau} \rangle$ with non-trivial momentum dependence arising from the unitary transformation $U_{\eta\tau}^s(\mathbf{p})$ (details in the SM).

We obtain two qualitatively different (b, α_R) SC phase diagrams depending on which interactions are dominant. In Fig. 1(a), the dominant interactions give the singlet extended s-wave state in the limit of vanishing SOC and $\mathbf{B}$, whereas in Fig. 1(b), this state would be the triplet f-wave state discussed above. For this reason, we refer to them, respectively, as the "singlet instability" and "triplet instability" phase diagrams. Note, however, that the SC states themselves are always a mixture of singlet and triplet for finite SOC and $\mathbf{B}$.

We first analyze the singlet-instability phase diagram, Fig. 1(a). Across the entire phase diagram, the gap at the $\pm K$ pockets is nearly isotropic. Along the $b = 0$ axis, the main effect of increasing the Rashba SOC α_R is to make $\Delta_{\Gamma\tau}(\mathbf{p})$ mildly anisotropic, due to the small admixture of the nodal triplet f-wave state. Importantly, no phase transition happens along this axis. In contrast, along the $\alpha_R = 0$ axis, a phase transition takes place to a nodal topological SC state for $b = b_P$, where $b_P \approx \Delta_{\Gamma1}$ corresponds roughly to the Pauli-limiting field [36, 37]. This phase transition, and the topological character of the resulting nodal SC state, were previously predicted in Ref. [17] and can be understood as a consequence of the vanishing of the Ising SOC along the six Γ-M directions, where the 12 nodes (6 for each Γ pocket) appear due to spins aligning with the magnetic field.

However, moving away from the $\alpha_R = 0$ axis, the Rashba SOC introduces a second spin-orbit energy scale that does not vanish along the Γ-M directions. As a result, even an infinitesimal Rashba SOC lifts the nodes and destroys the topological character of this state. The only exception is when $\mathbf{B}$ is aligned along one of the Γ-K directions: in this case, as we discuss in detail below, the system has a mirror symmetry that protects the four nodes located along the Γ-M direction perpendicular to $\mathbf{B}$ (while the other eight nodes are lifted). The result is a *crystalline* nodal topological SC phase, which remains stable provided that $b > \alpha_R p_F$. This behavior is illustrated in Fig. 3(a) and (b), which show the evolution of $\Delta_{\Gamma1}(\mathbf{p})$ as one moves along a cut (see inset) in the phase

diagram of Fig. 1(a) for $\mathbf{B}$ oriented along a direction different from Γ-K (panel a) or a direction coinciding with Γ-K (panel b).

We now move on to the triplet-instability phase diagram, displayed in Fig. 1(b). The region $b > \alpha_R p_F$ of the (b, α_R) phase diagram is very similar to that obtained for the singlet-instability case, except that the nodal topological SC state along the $\alpha_R = 0$ line occurs for arbitrarily small values of b, due to the absence of the Pauli limit in this regime [36, 37]. In contrast, along the $b = 0$ axis the phase diagram of Fig. 1(b) is quite distinct from that of Fig. 1(a). First, the nodes on the Γ pocket at $\alpha_R = b = 0$ are lifted due to a symmetry-allowed admixture with the sub-leading singlet state, resulting in an anisotropic gap. This is shown in Fig. 3(c), which presents the evolution of $\Delta_{\Gamma1}(\mathbf{p})$ along the $b = 0$ axis for increasing α_R (the gaps at $\pm K$ remain nearly isotropic). Note that to generate all symmetry-allowed terms, we include a small difference between the inner and outer DOS in the plots of Fig. 3, and show only $\Delta_{\Gamma1}$. As the difference in DOS is small, $\Delta_{\Gamma,-1}$ behaves very similarly.

Second, for a critical value of α_R, analyzing the gap equations beyond the linearized approximation (see SM), we find a phase transition to a chiral $p \pm ip$ superconducting state. This chiral state occurs because at large α_R and $b = 0$, the gap formally transforms as a two-dimensional irreducible representation of the relevant C_{3v} point group, and time reversal is spontaneously broken [38, 39]. While our calculations give a nodal gap $\Delta_{\Gamma\tau}(\mathbf{p})$ (shown in Fig. 3(d)), these nodes are not symmetry-enforced, and can be lifted by sub-leading terms not included in our model. This results in a gapped chiral topological SC with a Chern number of ± 6 (± 2 from the Γ pocket, and ± 4 from the $\pm K$ pockets), and gapless chiral edge modes resulting in a thermal Hall conductance $\kappa_{xy} = \pm 6 \left(\pi^2 k_B^2 / 3h \right) T$ [28]. This topological SC phase survives for some range of b, but our approach is insufficient to quantitatively obtain the phase boundary (see dashed lines in Fig. 1(b)).

Crystalline nodal topological superconductivity. Having established the existence of a nodal SC phase for large magnetic fields in the phase diagrams of Fig. 1, we now discuss its topological properties. As discussed in Refs. [40–43], two-dimensional nodal topological phases are stable only in the presence of certain symmetries, which guarantee both stability of the bulk nodes, and of the gapless flat-bands found at the edges. When $\alpha_R = 0$, the SC state has both particle-hole symmetry and an antiunitary time-reversal-like symmetry $\tilde{\mathcal{T}} = \mathcal{M}_z \mathcal{T} = i\sigma^x \mathcal{K}$, where $\mathcal{K}$ is complex conjugation, and σ^x acts on the spin index. Physically, $\tilde{\mathcal{T}}$ is a composition of time-reversal symmetry $\mathcal{T}$ and a reflection $\mathcal{M}_z$ with respect to the xy plane. $\tilde{\mathcal{T}}$ reverses the in-plane momentum and the z component of the spin, satisfying $\tilde{\mathcal{T}}^2 = 1$. This time-reversal-like symmetry places the system into symmetry class BDI [44, 45] and protects the 12 nodes of the superconducting gap on the two Γ pockets along the Γ-M lines, ensuring that the boundary flat bands cannot be
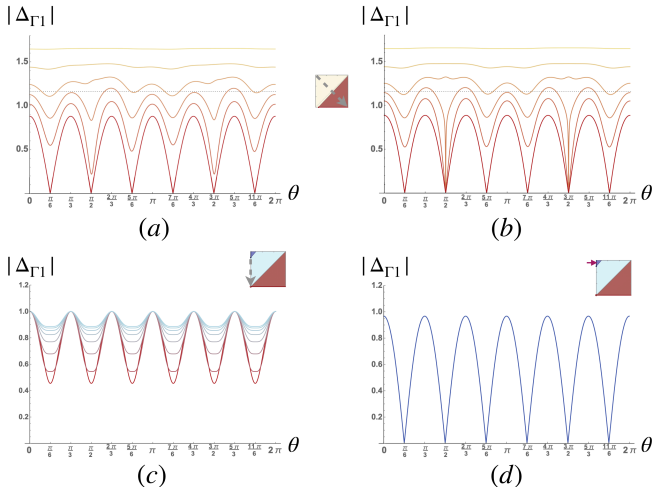
FIG. 3. Superconducting gap $\Delta_{\Gamma 1}$ at the outer Γ pocket, as a function of the angle θ with respect to the Γ-K direction, in various regions of the phase diagrams of Fig. 1 (for precise parameter values, see SM). Panels (a) and (b) correspond to the cuts across the phase diagram of Fig. 1(a) shown in the insets, with a magnetic field away from the Γ-K direction (panel (a)) and along (panel (b)) the Γ-K direction. Panels (c) and (d) correspond to cuts along the $b = 0$ axis of the phase diagram of Fig. 1(b), outside and inside the chiral SC phase, respectively (see insets). Note that the gap amplitudes have been rescaled for clarity, since they are not fixed by the linearized gap equations.
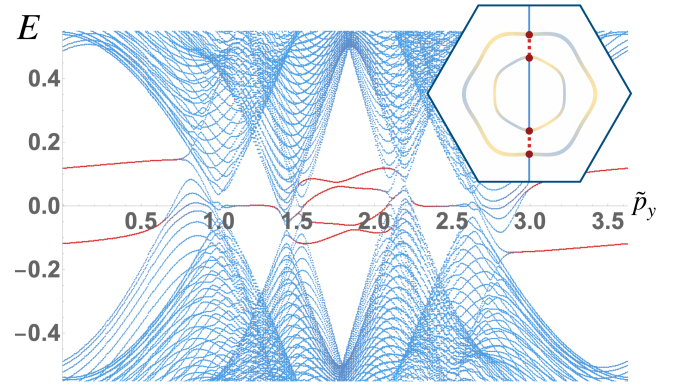

FIG. 4. Spectrum of the BdG Hamiltonian in the nodal topological crystalline SC phase on a $100 \times \infty$ unit cell strip with $\mathbf{B} = B\hat{x}$. Blue indicates bulk eigenstates, while red indicates eigenstates concentrated near the boundaries. $\tilde{p}_y = p_y + p_{y,\text{shift}}$ is a monotonic function of p_y that accounts for the shift of the Fermi surfaces. *Inset:* Position of the nodes (red dots) in the Brillouin zone. Dashed lines indicate how boundary flat bands connect the bulk nodes. For detailed parameter values, see SM.

gapped [22, 42]. However, a finite Rashba SOC breaks the $\tilde{\mathcal{T}}$ symmetry, implying that for generic in-plane field directions the system is in a fully gapped, topologically trivial SC phase with no protected zero-energy boundary states.

The notable exception is when $\mathbf{B}$ is parallel to one of the Γ-K directions: in this case, the system has a mirror symmetry that reflects about the plane perpendicular to $\mathbf{B}$. Combined with particle-hole symmetry, this mirror reflection can protect the four nodes in the reflection plane (see inset of Fig. 4)[43, 46]. For example, when $\mathbf{B}$ is parallel to the x axis, the mirror symmetry corresponds to a reflection with respect to the yz plane perpendicular to $\mathbf{B}$, which also flips the y and z components of spin: $\mathcal{M}_x = i\sigma^x R_{yz}$, where R_{yz} reflects $(x, y, z) \to (-x, y, z)$ and as above, σ^x acts on the physical spin indices. As discussed in the SM, for $\alpha_R p_F < b$ this symmetry forbids any fermion bilinears that can lift the nodes. This analysis is sufficient [43] to guarantee topological stability of the nodes; thus, the crystalline SC state is stable in a wide region of the phase diagrams of Fig. 1. We emphasize that the topological nature of the $\alpha_R \neq 0$ SC state is qualitatively different than of the $\alpha_R = 0$ SC state, as in the former case the symmetry that protects the SC state is not time-reversal-like, but a mirror symmetry of the crystal – hence the denomination crystalline topological SC. Note that in the presence of both b and α_R, the Fermi surfaces are no longer centered at zero momentum, and

thus the Cooper pairs have a finite center-of-mass momentum $\mathbf{p}_{\text{shift}}$, $\Delta_{\eta,\tau} \propto \langle c_{\eta,\mathbf{p}+\mathbf{p}_{\text{shift}},\tau} c_{\eta,-\mathbf{p}+\mathbf{p}_{\text{shift}},\tau} \rangle$.

A striking feature of the crystalline nodal topological SC phase is the existence of gapless flat-band boundary modes that are protected by the mirror symmetry. Fig. 4 shows the resulting Bogolyubov-de Gennes (BdG) spectrum on a $100 \times \infty$ unit cell strip with open zig-zag edges parallel to the $\hat{y}$ direction, and $\mathbf{B} = B\hat{x}$. Each state ψ_k is colored according to the inverse participation ratio $\sum_y |\psi_k(y)|^4$, such that the boundary flat bands are red while the delocalized bulk bands are blue. In this geometry, the boundary flat bands connect in a pairwise fashion the four gap nodes located along $k_x = 0$ (see the inset of Fig. 4). Importantly, these boundary states are pinned at zero energy by the mirror symmetry, after accounting for the finite-momentum pairing described above (details in the SM). In actual materials, the existence of both bulk nodes and zero-energy boundary states is guaranteed only if the relevant mirror reflection is an exact symmetry. As such, these may be sensitive to orientational defects in the crystal.

Concluding remarks: Our microscopic interacting model for NbSe$_2$ predicts multiple possible exotic superconducting phases in this material, tuned by the Rashba SOC α_R and the in-plane magnetic field B. Two different primary SC instabilities can be driven by purely electronic interactions: a singlet extended s-wave and a triplet f-wave SC state. The triplet instability supports a chiral topological SC state for small b and large α_R, and both instabilities support a crystalline nodal topological SC state for large b and small α_R. Interestingly, the topological properties of the latter phase depend crucially on the $\mathbf{B}$ field being aligned along one the Γ-K directions.

Although direct experimental detection of these topo-

logical SC states via their edge modes may be technically challenging, their indirect experimental manifestations should be accessible. For instance, because the chiral SC state transforms as a two-dimensional irreducible representation of the trigonal space group, it should be strongly affected by strain, with T_c splitting into 2 separate transitions under externally applied uniaxial strain [47]. As for the crystalline topological SC state, its extreme sensitivity to the field direction is expected to promote strongly anisotropic properties. Specifically, since the nature of the SC state changes as a function of the **B** direction, one expects pronounced six-fold anisotropies in the upper critical field and in the critical current. Such anisotropies should vary significantly as the Rashba SOC is changed.

[1] Y. Cao, A. Mishchenko, G. L. Yu, E. Khestanova, A. P. Rooney, E. Prestat, A. V. Kretinin, P. Blake, M. B. Shalom, C. Woods, J. Chapman, G. Balakrishnan, I. V. Grigorieva, K. S. Novoselov, B. A. Piot, M. Potemski, K. Watanabe, T. Taniguchi, S. J. Haigh, A. K. Geim, and R. V. Gorbachev, *Nano Letters*, Nano Letters **15**, 4914 (2015).

[2] J. T. Ye, Y. J. Zhang, R. Akashi, M. S. Bahramy, R. Arita, and Y. Iwasa, Science **338**, 1193 (2012).

[3] K. Taniguchi, A. Matsumoto, H. Shimotani, and H. Takagi, Applied Physics Letters **101**, 042603 (2012).

[4] X. Xi, H. Berger, L. Forró, J. Shan, and K. F. Mak, Phys. Rev. Lett. **117**, 106801 (2016).

[5] J. M. Lu, O. Zheliuk, I. Leermakers, N. F. Q. Yuan, U. Zeitler, K. T. Law, and J. T. Ye, Science **350**, 1353 (2015).

[6] Y. Saito, Y. Nakamura, M. S. Bahramy, Y. Kohama, J. Ye, Y. Kasahara, Y. Nakagawa, M. Onga, M. Tokunaga, T. Nojima, Y. Yanase, and Y. Iwasa, Nature Physics **12**, 144 EP (2015).

[7] X. Xi, Z. Wang, W. Zhao, J.-H. Park, K. T. Law, H. Berger, L. Forró, J. Shan, and K. F. Mak, Nature Physics **12**, 139 EP (2015).

[8] M. M. Ugeda, A. J. Bradley, Y. Zhang, S. Onishi, Y. Chen, W. Ruan, C. Ojeda-Aristizabal, H. Ryu, M. T. Edmonds, H.-Z. Tsai, A. Riss, S.-K. Mo, D. Lee, A. Zettl, Z. Hussain, Z.-X. Shen, and M. F. Crommie, Nature Physics **12**, 92 EP (2015).

[9] W. Shi, J. Ye, Y. Zhang, R. Suzuki, M. Yoshida, J. Miyazaki, N. Inoue, Y. Saito, and Y. Iwasa, Scientific Reports **5**, 12534 EP (2015).

[10] S. C. de la Barrera, M. R. Sinko, D. P. Gopalan, N. Sivadas, K. L. Seyler, K. Watanabe, T. Taniguchi, A. W. Tsen, X. Xu, D. Xiao, and B. M. Hunt, Nature Communications **9**, 1427 (2018).

[11] E. Navarro-Moratalla, J. O. Island, S. Mañas-Valero, E. Pinilla-Cienfuegos, A. Castellanos-Gomez, J. Quereda, G. Rubio-Bollinger, L. Chirolli, J. A. Silva-Guillén, N. Agraït, G. A. Steele, F. Guinea, H. S. J. van der Zant, and E. Coronado, Nature Communications **7**, 11043 EP (2016).

[12] B. T. Zhou, N. F. Q. Yuan, H.-L. Jiang, and K. T. Law, Phys. Rev. B **93**, 180501 (2016).

[13] N. F. Q. Yuan, B. T. Zhou, W.-Y. He, and K. T. Law, arXiv:1605.01847 (2016).

[14] E. Sohn, X. Xi, W.-Y. He, S. Jiang, Z. Wang, K. Kang, J.-H. Park, H. Berger, L. Forró, K. T. Law, J. Shan, and K. F. Mak, Nature Materials **17**, 504 (2018).

[15] S. Ilić, J. S. Meyer, and M. Houzet, Phys. Rev. Lett. **119**, 117001 (2017).

[16] P. A. Frigeri, D. F. Agterberg, A. Koga, and M. Sigrist, Phys. Rev. Lett. **92**, 097001 (2004).

[17] W.-Y. He, B. T. Zhou, J. J. He, N. F. Q. Yuan, T. Zhang, and K. T. Law, Communications Physics **1**, 40 (2018).

[18] E. Sosenko, J. Zhang, and V. Aji, Phys. Rev. B **95**, 144508 (2017).

[19] Y. Nakamura and Y. Yanase, Phys. Rev. B **96**, 054501 (2017).

[20] D. Möckli and M. Khodas, Phys. Rev. B **98**, 144518 (2018).

[21] D. Möckli and M. Khodas, arXiv:1902.02577 .

[22] M. H. Fischer, M. Sigrist, and D. F. Agterberg, Phys. Rev. Lett. **121**, 157003 (2018).

[23] M. Smidman, M. B. Salamon, H. Q. Yuan, and D. F. Agterberg, Reports on Progress in Physics **80**, 036501 (2017).

[24] N. F. Q. Yuan, K. F. Mak, and K. T. Law, Phys. Rev. Lett. **113**, 097001 (2014).

[25] R. Oiwa, Y. Yanagi, and H. Kusunose, Phys. Rev. B **98**, 064509 (2018).

[26] Y.-T. Hsu, A. Vaezi, M. H. Fischer, and E.-A. Kim, Nature Communications **8**, 14985 EP (2017).

[27] L. Wang, T. O. Rosdahl, and D. Sticlet, Phys. Rev. B **98**, 205411 (2018).

[28] N. Read and D. Green, Phys. Rev. B **61**, 10267 (2000).

[29] R. Oiwa, Y. Yanagi, and H. Kusunose, arXiv:1903.04830 .

[30] L. P. Gor'kov and E. I. Rashba, Phys. Rev. Lett. **87**, 037004 (2001).

[31] A. C. Potter and P. A. Lee, Phys. Rev. B **83**, 184520 (2011).

[32] E. Lake, C. Webb, D. A. Pesin, and O. A. Starykh, Phys. Rev. B **93**, 214516 (2016).

[33] A. V. Chubukov, M. Khodas, and R. M. Fernandes, Phys. Rev. X **6**, 041045 (2016).

[34] P. J. Hirschfeld, M. M. Korshunov, and I. I. Mazin, Reports on Progress in Physics **74**, 124508 (2011).

[35] T. V. Trevisan, M. Schütt, and R. M. Fernandes, Phys.

Rev. Lett. **121**, 127002 (2018).

[36] B. S. Chandrasekhar, Applied Physics Letters **1**, 7 (1962).

[37] A. M. Clogston, Phys. Rev. Lett. **9**, 266 (1962).

[38] K. V. Samokhin, Phys. Rev. B **92**, 174517 (2015).

[39] M. S. Scheurer, D. F. Agterberg, and J. Schmalian, npj Quantum Materials **2**, 9 (2017).

[40] A. P. Schnyder and S. Ryu, Phys. Rev. B **84**, 060504 (2011).

[41] M. Sato, Y. Tanaka, K. Yada, and T. Yokoyama, Phys. Rev. B **83**, 224511 (2011).

[42] S. Matsuura, P.-Y. Chang, A. P. Schnyder, and S. Ryu, New Journal of Physics **15**, 065001 (2013).

[43] C.-K. Chiu and A. P. Schnyder, Phys. Rev. B **90**, 205136 (2014).

[44] A. Altland and M. R. Zirnbauer, Phys. Rev. B **55**, 1142 (1997).

[45] S. Ryu, A. P. Schnyder, A. Furusaki, and A. W. W. Ludwig, New Journal of Physics **12**, 065010 (2010).

[46] M. Sato and Y. Ando, Reports on Progress in Physics **80**, 076501 (2017).

[47] C. W. Hicks, D. O. Brodsky, E. A. Yelland, A. S. Gibbs, J. A. N. Bruin, M. E. Barber, S. D. Edkins, K. Nishimura, S. Yonezawa, Y. Maeno, and A. P. Mackenzie, Science **344**, 283 (2014).

Supplementary Material for: "Crystalline nodal topological superconductivity in monolayer NbSe$_2$"

Daniel Shaffer,[1] Jian Kang,[2] F. J. Burnell,[1] and Rafael M. Fernandes[1]

[1]*School of Physics and Astronomy, University of Minnesota, Minneapolis, Minnesota 55455, USA*

[2]*National High Magnetic Field Laboratory, Florida State University, Tallahassee, Florida 32310, USA*

(Dated: April 12, 2019)

I. GAP EQUATIONS

The interactions presented in Eq. (2) of the main text can be expressed in the form:

$$H_{\text{Int}} = V_{\Gamma;\Gamma}^{\alpha'\beta';\alpha\beta}(\mathbf{p};\mathbf{k})\, d^\dagger_{\Gamma,\mathbf{p}\alpha} d^\dagger_{\Gamma,-\mathbf{p}\beta'} d_{\Gamma,\mathbf{k}\alpha'} d_{\Gamma,-\mathbf{k}\beta'} +$$
$$V_{\pm K;\pm K}^{\alpha'\beta';\alpha\beta}(\mathbf{p};\mathbf{k})\, d^\dagger_{\pm K,\mathbf{p}\alpha} d^\dagger_{\mp K,-\mathbf{p}\beta'} d_{\pm K,\mathbf{k}\alpha'} d_{\mp K,-\mathbf{k}\beta'} +$$
$$V_{\pm K;\mp K}^{\alpha'\beta';\alpha\beta}(\mathbf{p};\mathbf{k})\, d^\dagger_{\pm K,\mathbf{p}\alpha} d^\dagger_{\mp K,-\mathbf{p}\beta'} d_{\mp K,\mathbf{k}\alpha'} d_{\pm K,-\mathbf{k}\beta'} +$$
$$V_{\Gamma;\pm K}^{\alpha'\beta';\alpha\beta}(\mathbf{p};\mathbf{k})\, d^\dagger_{\pm K,\mathbf{p}\alpha} d^\dagger_{\mp K,-\mathbf{p}\beta'} d_{\Gamma,\mathbf{k}\alpha'} d_{\Gamma,-\mathbf{k}\beta'} + \text{h.c.}$$

$$\text{(S1)}$$

where we have left implicit the momenta of the fermion operators about each Fermi surface. Here, we will use the indices α and β for the spin indices; in the main text, we used s. Accounting for the anti-symmetric nature of the fermion operators (and including all Hermitian conjugates), the uniform part of the interactions can be separated into singlet and triplet interaction channels, as follows:

$$[V^s]_{\Gamma;\Gamma}^{\alpha'\beta';\alpha\beta} = g_1 (i\sigma^y)^{\alpha\beta}(i\sigma^y)^{\alpha'\beta'} \qquad \text{(S2)}$$
$$[V^s]_{\Gamma;\pm K}^{\alpha'\beta';\alpha\beta} = \pm g_4 (i\sigma^y)^{\alpha\beta}(i\sigma^y)^{\alpha'\beta'}$$
$$[V^s]_{\pm K;\pm K}^{\alpha'\beta';\alpha\beta} = \frac{1}{2}(g_2+g_3)(i\sigma^y)^{\alpha\beta}(i\sigma^y)^{\alpha'\beta'}$$
$$[V^t]_{\pm K;\pm K}^{\alpha'\beta';\alpha\beta} = \frac{1}{2}(g_2-g_3)\sum_{i=x,y,z}(\sigma^i i\sigma^y)^*_{\alpha\beta}(\sigma^i i\sigma^y)^{\alpha'\beta'}$$

Since $V_{K,K}$ and $V_{K,-K}$ are related by interchanging the spin indices α',β', combined with an overall minus sign for interchanging two fermion operators, in this representation we have

$$[V^s]_{\pm K;\mp K}^{\alpha'\beta';\alpha\beta} = [V^s]_{\pm K;\pm K}^{\alpha'\beta';\alpha\beta}$$
$$[V^t]_{\pm K;\mp K}^{\alpha'\beta';\alpha\beta} = -[V^t]_{\pm K;\pm K}^{\alpha'\beta';\alpha\beta} \qquad \text{(S3)}$$

From Eq. (S2), we see that $V_{\pm K,\pm K}$ (and thus $V_{\pm K,\mp K}$) have contributions in both the singlet channel (labeled s) and the triplet channel (labeled t), while for momentum-independent interactions, $V_{\Gamma,\Gamma}$ and $V_{\Gamma,K}$ have contributions only in the singlet channel. In addition to these momentum independent interactions, in order to ensure that the gap on the Γ pocket does not artificially vanish in the triplet regime, we also include weak (but symmetry-allowed) momentum dependent interactions, so $V(\mathbf{p};\mathbf{k}) = V^s + V^t(\mathbf{p};\mathbf{k})$:

$$[V^t(\mathbf{p};\mathbf{k})]_{\Gamma;\Gamma}^{\alpha'\beta';\alpha\beta} = g_1^t \cos(3\theta_\mathbf{k})\cos(3\theta_\mathbf{p})(i\sigma^y)^{\alpha\beta}(i\sigma^y)^{\alpha'\beta'}$$
$$[V^t(\mathbf{p};\mathbf{k})]_{\Gamma;\pm K}^{\alpha'\beta';\alpha\beta} = \pm\sqrt{2}g_4^t \cos(3\theta_\mathbf{k})(\sigma^i i\sigma^y)^*_{\alpha\beta}(\sigma^i i\sigma^y)^{\alpha'\beta'}$$

$$\text{(S4)}$$

where $\theta_\mathbf{k}$ refers to the angle of the momentum on the Γ pocket. We emphasize that we take $|g_i^t| \ll |g_i|$, such that these interactions have a negligible effect on whether the system enters the singlet or triplet regime.

Next, we express the interactions in terms of the eigenstates of the single body Hamiltonian with Ising SOC, Rashba SOC, and magnetic field. The non-interacting Hamiltonian is diagonalized by performing a unitary transformation

$$c_{\eta,\mathbf{p}\tau} = U_{\eta\tau}^\alpha(\mathbf{p})d_{\eta,\mathbf{p}\alpha} \qquad \text{(S5)}$$

where $\tau = +1$ (-1) on the outer (inner) spin-split Fermi surface, $\alpha = 1$ (-1) for spin up (spin down), and we have defined

$$U_{\Gamma\tau}^\alpha(\mathbf{p}) = \sqrt{\frac{\delta_\Gamma + \tau\alpha(2\lambda p^3 \cos 3\theta_\mathbf{p})}{2\delta_\Gamma}}\left(\tau e^{-i\phi}\right)^{\frac{1+\alpha}{2}}$$
$$U_{\pm K\tau}^\alpha(\mathbf{p}) = \sqrt{\frac{\delta_K \pm \tau\alpha\beta_I}{2\delta_K}}\left(\tau e^{-i\phi}\right)^{\frac{1+\alpha}{2}} \qquad \text{(S6)}$$

Here

$$\delta_\Gamma = \sqrt{(2\lambda p^3 \cos(3\theta))^2 + (\alpha_R p_y + b_x)^2 + (\alpha_R p_x - b_y)^2}$$
$$\delta_K = \sqrt{\beta_I^2 + (\alpha_R p_y + b_x)^2 + (\alpha_R p_x - b_y)^2}$$
$$e^{i\phi} = \frac{\alpha_R p_y + b_x + i(-\alpha_R p_x + b_y)}{\sqrt{(\alpha_R p_y + b_x)^2 + (\alpha_R p_x - b_y)^2}} \qquad \text{(S7)}$$

where $\mathbf{p}$ is the momentum at the Fermi surface centered at Γ or $\pm K$, $\mathbf{b} \equiv g_L \mu_B \mathbf{B}$, α_R is the Rashba SOC parameter, β_I is the Ising SOC parameter at K, and λ is the Ising SOC parameter at Γ. Projecting the interactions onto the spin-split Fermi surfaces gives

$$H_{\text{Int}} = \tilde{V}_{\Gamma;\Gamma}^{\tau,\tau'}\, c^\dagger_{\Gamma\tau} c^\dagger_{\Gamma\tau} c_{\Gamma\tau'} c_{\Gamma\tau'} +$$
$$\tilde{V}_{\pm K,\pm K}^{\tau,\tau'}\, c^\dagger_{\pm K\tau} c^\dagger_{\mp K\tau} c_{\pm K\tau'} c_{\mp K\tau'} +$$
$$\tilde{V}_{\pm K,\mp K}^{\tau,\tau'}\, c^\dagger_{\pm K\tau} c^\dagger_{\mp K\tau} c_{\mp K\tau'} c_{\pm K\tau'} +$$
$$\tilde{V}_{\Gamma\pm K}^{\tau,\tau'}\, c^\dagger_{\pm K\tau} c^\dagger_{\mp K\tau} c_{\Gamma\tau'} c_{\Gamma\tau'} \qquad \text{(S8)}$$

with (repeated indices are summed implicitly in the expression below):

$$\tilde{V}_{\eta,\eta'}^{\tau,\tau'}(\mathbf{p},\mathbf{k}) =$$
$$= U_{\eta\tau}^{\alpha}(\mathbf{p})U_{-\eta\tau}^{\beta}(-\mathbf{p})U_{\eta'\tau'}^{\alpha'*}(\mathbf{k})U_{-\eta'\tau'}^{\beta'*}(-\mathbf{k})V_{\eta,\eta'}^{\alpha\beta;\alpha'\beta'}(\mathbf{p};\mathbf{k}) \tag{S9}$$

where we define the pocket index $\eta = K, -K, \Gamma$, and use the convention that $-\Gamma \equiv \Gamma$. Note that after this projection, all interactions are momentum-dependent.

The superconducting gaps are given by:

$$\Delta_{\Gamma,\tau}(\mathbf{p}) \propto \langle c_{\Gamma,\mathbf{p}\tau}c_{\Gamma,-\mathbf{p}\tau}\rangle$$
$$\Delta_{K,\tau}^{(\epsilon,-\epsilon)}(\mathbf{p}) \propto \langle c_{\epsilon K,\mathbf{p}\tau}c_{-\epsilon K,-\mathbf{p}\tau}\rangle \tag{S10}$$

where the momentum $\mathbf{p}$ is measured with respect to the center of the Fermi pocket in question in all cases, and $\epsilon = \pm 1$. For convenience of notation, we define $\Delta_{\epsilon K,\tau}(\mathbf{p}) \equiv \Delta_{K,\tau}^{(\epsilon,-\epsilon)}(\mathbf{p})$. Because particle-hole symmetry imposes $\Delta_{-K,\tau}(\mathbf{p}) = -\Delta_{K,\tau}(-\mathbf{p})$, it is sufficient to determine $\Delta_{K,\tau}$ only.

Ignoring the coupling between the inner and outer Fermi surfaces centered at the high-symmetry points, the linearized gap equation becomes:

$$\Delta_{\eta,\tau}(\mathbf{p}) = -2\ln\frac{\Lambda}{T_c}\sum_{\eta',\tau'}N_{\eta'\tau'}\oint \tilde{V}_{\eta,\eta'}^{\tau,\tau'}(\mathbf{p};\mathbf{k})\Delta_{\eta',\tau'}(\mathbf{k})\frac{d\theta_{\eta',\mathbf{k}}}{2\pi} \tag{S11}$$

where $\theta_{\eta',\mathbf{k}}$ is the angle along the τ' Fermi surface relative to the center of the pocket η' (below we simply use θ when this is clear from context), with $N_{\eta'\tau'}$ being the corresponding density of states. The projected interactions can be expressed conveniently as:

$$\tilde{V}_{\eta,\eta'}^{\tau,\tau'}(\mathbf{p},\mathbf{k}) = \sum_{\mu=0,x,y,z}g_{\eta,\eta'}^{(\mu)}Q_{\eta,\tau}^{(\mu)}(\mathbf{p})Q_{\eta',\tau'}^{(\mu)*}(\mathbf{k}) \tag{S12}$$

where $g_{\eta,\eta'}^{(\mu)}$ are constants independent of $\mathbf{p}$ and $\mathbf{k}$. Explicitly, $g_{\Gamma,\Gamma}^{(0)} = g_1$, $g_{\Gamma,\pm K}^{(0)} = g_{\pm K,\Gamma}^{(0)} = g_4$, $g_{\pm K,\pm K}^{(0)} = g_{\pm K,\mp K}^{(0)} = \frac{g_2+g_3}{2}$, and for $i = x, y, z$ we have $g_{\Gamma,\Gamma}^{(i)} = g_1^t$, $g_{\Gamma,\pm K}^{(i)} = g_{\pm K,\Gamma}^{(i)} = g_4^t$, $g_{\pm K,\pm K}^{(i)} = g_{\pm K,\mp K}^{(i)} = \frac{g_2-g_3}{2}$. We can then parametrize $\Delta_{\eta,\tau}(\mathbf{k}) = \sum_{\mu}D_{\eta\tau}^{(\mu)}Q_{\eta,\tau}^{(\mu)}(\mathbf{p})$ where $D_{\eta\tau}^{(\mu)}$ are gap coefficients independent of momentum to be determined. Explicitly,

$$Q_{\eta,\tau}^{(0)}(\mathbf{p}) = \sum_{\alpha\beta}(i\sigma^y)_{\alpha\beta}U_{\eta\tau}^{\alpha}(\mathbf{p})U_{-\eta\tau}^{\beta}(-\mathbf{p}) \tag{S13}$$

$$Q_{\pm K,\tau}^{(i)}(\mathbf{p}) = \pm\sum_{\alpha\beta}(i\sigma^i i\sigma^y)_{\alpha\beta}U_{K\tau}^{\alpha}(\mathbf{p})U_{-K\tau}^{\beta}(-\mathbf{p})$$

$$Q_{\Gamma,\tau}^{(i)}(\mathbf{p}) = \sqrt{2}\cos(3\theta_{\mathbf{p}})\sum_{\alpha\beta}(i\sigma^i i\sigma^y)_{\alpha\beta}U_{\Gamma\tau}^{\alpha}(\mathbf{p})U_{\Gamma\tau}^{\beta}(-\mathbf{p})$$

The additional factors of i in the last two expressions are taken for convenience, making the $D_{\eta\tau}^{(\mu)}$ coefficients real when the density of states are equal on inner and outer

Fermi surfaces. The structure of the reduced equation implies that we can take $D_{\eta\tau}^{(\mu)} = D_{\eta-\tau}^{(\mu)} \equiv D_{\eta}^{(\mu)}$, and we thus drop the τ index on D herafter. Moreover, particle-hole symmetry enforces $D_K^{(\mu)} = D_{-K}^{(\mu)}$, consistent with the fact that $\Delta_{-K,\tau}(\mathbf{p}) = -\Delta_{K,\tau}(-\mathbf{p})$.

Plugging the form (S13) back into the gap equation (S11) yields the reduced gap equation

$$D_{\eta}^{(\mu)} = \sum_{\eta'\mu'}g_{\eta,\eta'}^{(\mu)}f_{(\mu')}^{(\mu)\eta'}D_{\eta'}^{(\mu')} \tag{S14}$$

or more explicitly

$$D_{\Gamma}^{(0)} = \sum_{\mu}\left(g_1 f_{(\mu)}^{(0)\Gamma}D_{\Gamma}^{(\mu)} + 2g_4 f_{(\mu)}^{(0)K}D_K^{(\mu)}\right) \tag{S15}$$

$$D_K^{(0)} = \sum_{\mu}\left(g_4 f_{(\mu)}^{(0)\Gamma}D_{\Gamma}^{(\mu)} + (g_2+g_3)f_{(\mu)}^{(0)K}D_K^{(\mu)}\right)$$

$$D_{\Gamma}^{(i)} = \sum_{\mu}\left(g_1^t f_{(\mu)}^{(i)\Gamma}D_{\Gamma}^{(\mu)} + 2g_4^t f_{(\mu)}^{(i)K}D_K^{(\mu)}\right)$$

$$D_K^{(i)} = \sum_{\mu}\left(g_4^t f_{(\mu)}^{(i)\Gamma}D_{\Gamma}^{(\mu)} + (g_2-g_3)f_{(\mu)}^{(i)K}D_K^{(\mu)}\right)$$

where $\mu = 0, x, y, z$, and form factors $f_{(\mu)}^{(\mu')\eta}$ given by:

$$f_{(\mu')}^{(\mu)\eta} = -2\ln\frac{\Lambda}{T_c}\oint\sum_{\tau}N_{\eta\tau}Q_{\eta\tau}^{(\mu)*}Q_{\eta\tau}^{(\mu')}\frac{d\theta_{\eta,\mathbf{k}}}{2\pi} \tag{S16}$$

Note that due to the SOC the singlet and triplet channels do not decouple in general, and the superconducting gaps are neither spin singlet nor spin triplet. Eq. (S15) can be expressed as an 8×8 matrix equation, leading to 8 possible superconducting solutions, of which we choose the one with the highest T_c. The solutions can be found analytically when either the magnetic field or Rashba SOC is absent, but otherwise the equations have to be solved numerically.

To define the singlet and triplet instability regimes discussed in the main text, we consider the limit of no SOC and magnetic field. In this case, the (0) term reduces to the usual singlet gap, while (i) reduce to components of the triplet gap with d vector aligned along $i = x, y, z$. We define a dominant singlet (dominant triplet) instability to occur when the largest eigenvalue of the matrix equation (S15) is for the spin singlet (spin triplet) gap. The transition temperature for each channel is given by the condition that the corresponding eigenvalue of the gap equation equals 1. This yields $T_c^{(a)} = \Lambda\exp(\frac{-1}{2N\gamma^{(a)}})$, where N is the DOS of all bands (assumed to be equal), Λ is the upper energy cutoff, and:

$$\gamma^{(s)} = -g_1 - g_2 - g_3 + \sqrt{(g_1 - g_2 - g_3)^2 + 8g_4^2} \tag{S17}$$

in the singlet channel and

$$\gamma^{(t)} = g_3 - g_2 + |g_2 - g_3| \tag{S18}$$

in the triplet channel. Thus, for repulsive interactions, a SC state is realized when the the inter-band repulsions g_3 and g_4 dominate over the intraband repulsions g_1 and g_2. In this case, the singlet instability dominates for large g_4, while the triplet instability dominates for large g_3.

Fig. 3 in the main text plots solutions of the gap equations in different regimes. In panels (a) and (b), the parameters were chosen to be $\lambda/\beta_I = 0.6$, as well as $g_2 = 1.2$, $g_3 = 0.8$, $g_4 = 2$, $g_1^t = 0.2$ and $g_4^t = 0.1$ (all gs are given in units of the arbitrary positive interaction g_1). The magnetic field angle with respect to the Γ-K direction was set to be $\vartheta = 2\pi/25$ and 0 for (a) and (b), respectively. In panels (c) and (d), we took instead $g_3 = 4.2$. We also took the inner and outer densities of states to differ by ten percent in all panels; this ensures that the symmetry allowed mixings between the singlet and triplet channels are present in our solutions.

II. SPONTANEOUS TIME-REVERSAL SYMMETRY BREAKING

As discussed in the main text, for large enough α_R and $b = 0$, the triplet-instability phase diagram displays spontaneous time-reversal symmetry breaking, resulting in a chiral $p \pm ip$ superconducting phase. To show that indeed time-reversal symmetry is broken in this phase, we need to go beyond the linearized gap equations of the previous section. Note that in the basis (S5) we are working with, at $b = 0$ TRS acts as $\mathcal{T}c_{\eta,\mathbf{p}\tau}\mathcal{T}^{-1} = i\tau e^{i\theta}c_{-\eta,-\mathbf{p}\tau}$, which means that it takes the term $\Delta_{\eta\tau}(\mathbf{p})c_{\eta,\mathbf{p}\tau}^\dagger c_{-\eta,-\mathbf{p}\tau}^\dagger$ to $-e^{-2i\theta}\Delta_{\eta\tau}^*(\mathbf{p})c_{\eta,\mathbf{p}\tau}^\dagger c_{-\eta,-\mathbf{p}\tau}^\dagger$. Taking $\Delta_{\eta\tau}(\mathbf{p}) = e^{i\Phi_{\eta\tau}(\mathbf{p})}|\Delta_{\eta\tau}(\mathbf{p})|$, TRS is satisfied iff $e^{i\Phi_{\eta\tau}(\mathbf{p})} = \pm i e^{-i\theta}$.

Assuming equal densities of states on inner and outer Fermi surfaces, for $b = 0$ the different μ in the reduced gap equation (S15) are not coupled, and we obtain a solution to the gap equation for each $\mu = 0, x, y, z$. We express these solutions in terms of $\Delta_{\eta,\tau}^{(\mu)}(\mathbf{p}) \equiv D_{\eta\tau}^{(\mu)}Q_{\eta,\tau}^{(\mu)}(\mathbf{p})$. Explicitly, for $b = 0$,

$$\Delta_{\Gamma\tau}^{(0)}(\mathbf{p}) = \tau i e^{-i\theta}D_\Gamma^{(0)} \tag{S19}$$

$$\Delta_{\pm K\tau}^{(0)}(\mathbf{p}) = \tau i e^{-i\theta}D_K^{(0)}$$

$$\Delta_{\Gamma\tau}^{(z)}(\mathbf{p}) = \sqrt{2}i e^{-i\theta}\cos^2 3\theta \frac{\lambda p_F^3}{\delta_\eta(\mathbf{p})}D_\Gamma^{(z)}$$

$$\Delta_{\pm K\tau}^{(z)}(\mathbf{p}) = \pm i e^{-i\theta}\frac{\beta_I}{\delta_\eta(\mathbf{p})}D_K^{(z)}$$

$$\Delta_{\Gamma\tau}^{(x)}(\mathbf{p}) = \sqrt{2}i e^{-i\theta}\sin\theta\,\cos 3\theta \frac{\alpha_R p_F}{\delta_\eta(\mathbf{p})}D_\Gamma^{(x)}$$

$$\Delta_{\pm K\tau}^{(x)}(\mathbf{p}) = \pm i e^{-i\theta}\sin\theta\,\frac{\alpha_R p_F}{\delta_\eta(\mathbf{p})}D_K^{(x)}$$

$$\Delta_{\Gamma\tau}^{(y)}(\mathbf{p}) = \sqrt{2}i e^{-i\theta}\cos\theta\,\cos 3\theta \frac{\alpha_R p_F}{\delta_\eta(\mathbf{p})}D_\Gamma^{(y)}$$

$$\Delta_{\pm K\tau}^{(y)}(\mathbf{p}) = \pm i e^{-i\theta}\cos\theta\,\frac{\alpha_R p_F}{\delta_\eta(\mathbf{p})}D_K^{(y)}$$

The key point is that the (x) and (y) solutions are degenerate, i.e. have the same T_c. Formally, they belong to the 2D E irrep of C_{3v}, the relevant point group in this regime. We therefore associate these two solutions with p_x-wave and p_y-wave states. We now need to establish whether all of the $D_\eta^{(x)}$ and $D_\eta^{(y)}$ are non-zero, and if so, what their relative phase is. Instead of solving the full non-linear gap equations, it is sufficient to focus on the quartic term of the Ginzburg-Landau free energy. To obtain it, we start with the Bogolyubov-Gor'kov Hamiltonian:

$$H = -\frac{1}{4}\sum_{\substack{\mathbf{p}\eta\tau \\ \mathbf{k}\eta'\tau'}} \Delta_{\eta\tau}^*(\mathbf{p})\left(\tilde{V}^{-1}(\mathbf{p};\mathbf{k})\right)_{\eta\tau}^{\eta'\tau'}\Delta_{\eta'\tau'}(\mathbf{k}) + \frac{1}{2}\sum_{\mathbf{p}\eta\tau}\Psi_{\mathbf{p}\eta\tau}^\dagger\mathcal{H}_{\eta\tau}(\mathbf{p})\Psi_{\mathbf{p}\eta\tau} + \frac{1}{2}\sum_{\mathbf{p}\eta\tau}\xi_{\eta\tau}(\mathbf{p}) \tag{S20}$$

where we use the Nambu-Gor'kov representation $\Psi_{\eta\tau}(\mathbf{p}) = (c_{\eta,\mathbf{p}\tau}, c_{-\eta,-\mathbf{p}\tau}^\dagger)^T$ and defined the Bogoliubov-de Gennes (BdG) Hamiltonian

$$\mathcal{H}_{\eta\tau}(\mathbf{p}) = \begin{pmatrix} \xi_{\eta\tau}(\mathbf{p}) & \Delta_{\eta\tau}(\mathbf{p}) \\ \Delta_{\eta\tau}^*(\mathbf{p}) & -\xi_{-\eta\tau}(-\mathbf{p}) \end{pmatrix}. \tag{S21}$$

Note that when TRS is broken, $\xi_{-\eta\tau}(-\mathbf{p}) \neq \xi_{\eta\tau}(\mathbf{p})$ in general. The BdG spectrum is given by the eigenvalues of the BdG Hamiltonian, one of which is

$$E_{\eta\tau}(\mathbf{p}) = \frac{\xi_{\eta\tau}(\mathbf{p}) - \xi_{-\eta\tau}(-\mathbf{p})}{2} + \sqrt{\left(\frac{\xi_{\eta\tau}(\mathbf{p}) + \xi_{-\eta\tau}(-\mathbf{p})}{2}\right)^2 + |\Delta_{\eta\tau}(\mathbf{p})|^2} \equiv \xi_{a\eta\tau}(\mathbf{p}) + \sqrt{\xi_{s\eta\tau}(\mathbf{p})^2 + |\Delta_{\eta\tau}(\mathbf{p})|^2} \tag{S22}$$

and the second is fixed by particle-hole symmetry to be $-E_{-\eta\tau}(-\mathbf{p})$. Using the fact that

$$\det\left[-i\omega + \mathcal{H}_{\eta\tau}(\mathbf{p})\right] = (-i\omega + E_{\eta\tau}(\mathbf{p}))(-i\omega - E_{-\eta\tau}(-\mathbf{p})) \tag{S23}$$

we obtain the Ginzburg-Landau free energy:

$$\mathcal{F} = -2T\sum_{\mathbf{p}\eta\tau}\ln\left[2\cosh\left(\frac{\beta E_{\eta\tau}(\mathbf{p})}{2}\right)\right] + \mathcal{F}_0\left(|\Delta_{\eta\tau}|^2\right) \tag{S24}$$

where in the last step we assumed $b = 0$, so $\xi_{\eta\tau}(-\mathbf{p}) = \xi_{\eta\tau}(\mathbf{p})$. The contribution $\mathcal{F}_0\left(|\Delta_{\eta\tau}|^2\right)$ comes from the decoupling of the interaction; because it is purely quadratic in the gaps, it is inconsequential for our analysis.

Expanding the free energy in powers of the gap function, we obtain, in quartic order:

$$\mathcal{F}^{(4)} = \frac{7\zeta(3)}{32\pi^2 T^2} \sum_{\eta\tau} \int N_{\eta\tau} |\Delta_{\eta\tau}(\mathbf{p})|^4 \frac{d\theta_{\mathbf{p}}}{2\pi} \qquad \text{(S25)}$$

where $\zeta(x)$ is the Riemann zeta function. Substituting the general form of the gap function:

$$\Delta_{\Gamma\tau}(\mathbf{p}) = \sqrt{2}ie^{-i\theta}\cos 3\theta \frac{\alpha_R p_F}{\delta_\eta(\mathbf{p})} \left(D_\Gamma^{(x)}\cos\theta + D_\Gamma^{(y)}\sin\theta\right) \qquad \text{(S26)}$$

$$\Delta_{\pm K\tau}(\mathbf{p}) = \pm ie^{-i\theta}\frac{\alpha_R p_F}{\delta_\eta(\mathbf{p})} \left(D_K^{(x)}\cos\theta + D_K^{(y)}\sin\theta\right) \qquad \text{(S27)}$$

and approximating $\frac{\alpha_R p_F}{\delta_\eta(\mathbf{p})} \approx 1$ (which is valid as long as $\alpha_R p_F \gg \lambda p_F^3$), we obtain:

$$\mathcal{F}^{(4)} = \frac{7\zeta(3)}{1024\pi^2 T^2} \sum_{\eta\tau} N_{\eta\tau} \left[3\left(\left|D_\eta^{(x)}\right|^2 + \left|D_\eta^{(y)}\right|^2\right)^2\right. \qquad \text{(S28)}$$

$$\left. -4\left|D_\eta^{(x)}\right|^2 \left|D_\eta^{(y)}\right|^2 \sin^2\phi_{xy}\right]$$

where ϕ_{xy} is the relative phase between $D_\eta^{(x)}$ and $D_\eta^{(y)}$. A straightforward minimization gives $\phi_{xy} = \pm\frac{\pi}{2}$, which implies that the ground state is a $p \pm ip$ superconducting phase. Note that while the resulting $\Delta_{\Gamma\tau}(\mathbf{p})$ is actually nodal, there is an additional symmetry allowed term $\Delta^{(3)} = e^{3i\theta}$ that belongs to the same E irreducible representation which lifts the nodes.

III. TOPOLOGICAL SUPERCONDUCTIVITY

In the main text, we predicted two types of topological superconducting phases in NbSe$_2$ beyond the nodal topological superconductor at large in-plane magnetic fields previously discussed in the literature [17]. These were (1) a fully gapped, chiral superconductor with total Chern number 6 at large Rashba SOC similar to that recently predicted in MoS$_2$ [29], and (2) a crystalline nodal topological SC at large in-plane magnetic fields oriented along the Γ-K lines. Here we support these claims by calculating the Chern number of the time-reversal breaking superconductor, and discussing in more depth how symmetry protects the nodes and zero-energy boundary flat-bands of the crystalline nodaltopological SC.

Chern number

The Chern number of a 2D material is given by

$$Ch = \frac{1}{2\pi} \int_{BZ} \mathbf{F}_{\eta\tau}(\mathbf{p}) \cdot d^2\mathbf{p} \qquad \text{(S29)}$$

where the Berry curvature vector is given by

$$\mathbf{F}_{\eta\tau}(\mathbf{p}) = \sum_{\eta\tau} \boldsymbol{\nabla} \times \mathbf{A}_{\eta\tau}(\mathbf{p}) \qquad \text{(S30)}$$

with $\mathbf{A}_{\eta\tau}(\mathbf{p})$ the usual Berry connection associated with the occupied band only. For a superconductor, the Berry connection is defined in terms of the normalized eigenvectors of the BdG Hamiltonian (S21): $\Upsilon_{\eta\tau}(\mathbf{p}) = u_{\eta\tau}(\mathbf{p})c_{\eta,\mathbf{p}\tau} + v_{\eta\tau}(\mathbf{p})c^\dagger_{-\eta,-\mathbf{p}\tau}$, via

$$A_{\eta\tau}(\mathbf{p}) = i\langle\Upsilon_{\eta\tau}(\mathbf{p})|\nabla_{\mathbf{p}}|\Upsilon_{\eta\tau}(\mathbf{p})\rangle. \qquad \text{(S31)}$$

In our case, the $c_{\eta,\mathbf{p}\tau}$ operators may carry a nontrivial Berry phase due to the changing orientation of the associated spin. One should therefore consider $|\Upsilon_{\eta\tau}(\mathbf{p})\rangle$ as a four component eigenvector in a basis of Nambu-Gor'kov 4-spinors $\Psi_{\eta\tau}^{(4)}(\mathbf{p}) = (d_{\eta,\mathbf{p}\uparrow}, d_{\eta,\mathbf{p}\downarrow}, d^\dagger_{-\eta,-\mathbf{p}\uparrow}, d^\dagger_{-\eta,-\mathbf{p}\downarrow})^T$. Since

$$c_{\eta,\mathbf{p}\tau} = U_{\eta\tau}^\alpha(\mathbf{p})d_{\eta,\mathbf{p}\alpha} \qquad \text{(S32)}$$

we thus have

$$|\Upsilon_{\eta\tau}\rangle = \begin{pmatrix} U_{\eta\tau}^1(\mathbf{p})u_{\eta\tau}(\mathbf{p}) \\ U_{\eta\tau}^{-1}(\mathbf{p})u_{\eta\tau}(\mathbf{p}) \\ U_{-\eta\tau}^{1*}(-\mathbf{p})v_{\eta\tau}(\mathbf{p}) \\ U_{-\eta\tau}^{-1*}(-\mathbf{p})v_{\eta\tau}(\mathbf{p}) \end{pmatrix}. \qquad \text{(S33)}$$

where using the same notation as (S22) we have

$$u_{\eta\tau}(\mathbf{p}) = \frac{\xi_{s\eta\tau} - E_{\eta\tau}(\mathbf{p})}{\sqrt{(\xi_{s\eta\tau} - E_{\eta\tau}(\mathbf{p}))^2 + |\Delta_{\eta\tau}(\mathbf{p})|^2}} \qquad \text{(S34)}$$

$$v_{\eta\tau}(\mathbf{p}) = \frac{\Delta_{\eta\tau}(\mathbf{p})}{\sqrt{(\xi_{s\eta\tau} - E_{\eta\tau}(\mathbf{p}))^2 + |\Delta_{\eta\tau}(\mathbf{p})|^2}} \qquad \text{(S35)}$$

Below we calculate the Chern number for $b = 0$ and nonzero α_R only, in which case $U_{\eta\tau}^1(\mathbf{p}) = -i\left|U_{\eta\tau}^1(\mathbf{p})\right|e^{-i\theta_{\eta,\mathbf{p}}}$ where $\theta_{\eta,\mathbf{p}}$ is the angle of the momentum $\mathbf{p}$ measured relative to the center of the Fermi pocket η. Defining $\Delta_{\eta\tau}(\mathbf{p}) = |\Delta_{\eta\tau}(\mathbf{p})|e^{i\Phi_{\eta\tau}(\mathbf{p})}$, we find that in this regime the Berry connection associated with the pocket η is

$$A_{\eta\tau}(\mathbf{p}) = \left|U_{\eta\tau}^1(\mathbf{p})\right|^2 \nabla\theta_{\eta\mathbf{p}} - |v_{\eta\tau}(\mathbf{p})|^2 (\nabla\Phi_{\eta\tau}(\mathbf{p}) + \nabla\theta_{\eta\mathbf{p}}) \qquad \text{(S36)}$$

For the two TRS-breaking linear combinations $p + ip$ ($p - ip$) that we found above, $\Phi_{\eta\tau} = 0$ ($\Phi_{\eta\tau} = -2\theta_\eta$) respectively, on both Γ and $\pm K$ pockets. To obtain the Chern number we insert these expressions into (S36), and integrate over an annulus around each component of the

Fermi surface. Although in principle the integral in Eq. (S29) should be carried out over the entire Brillouin zone, in practice only this region proximate to the Fermi surface contributes. To evaluate these integrals, we assume that the gap function is constant in some region around the FS, and completely vanishing in regions sufficiently far from the FS, with a phase independent of the radial direction p, and take $\left|U_{\eta\tau}^1(\mathbf{p})\right|$ to be independent of p. Finally, observe that $v_{\eta\tau}$ changes rapidly from 0 to 1 in the vicinity of the Fermi surface. For the pocket η, we therefore obtain:

$$Ch_\eta = \frac{1}{2\pi} \int (F_{\eta\tau}(\mathbf{p}))_{p\theta}\, dp\, d\theta = \frac{1}{2\pi} \int \partial_p (A_{\eta\tau}(\mathbf{p}))_\theta\, dp\, d\theta \tag{S37}$$

$$= \frac{1}{2\pi} \left[\int (A_{\eta\tau}(\mathbf{p}))_\theta\, d\theta \right]_{p=0}^{p=\infty} = -\frac{1}{2\pi} \left[\Phi_{\eta\tau}(\mathbf{p}) + \theta_{\eta,\mathbf{p}} \right]_0^{2\pi} \tag{S38}$$

where the integrals over θ and p are understood to be over the tangential and normal directions in a disk including the Fermi surface of the η pocket, respectively. This gives a net Chern number of ± 6, with a total contribution of ± 4 from the $\pm K$ pockets, and of ± 2 from the Γ pocket .

Symmetry Protected Crystalline Nodal Phase

Here we show using a general symmetry analysis that in the presence of a mirror reflection symmetry the nodes lying on the reflection plane perpendicular to the sample plane indeed cannot be lifted provided that $b > \alpha_R p_F$. Note that a pair of nodes touch when $b = \alpha_R p_F$ and there is a topological phase transition into a nodeless phase at $b < \alpha_R p_F$. We take the magnetic field to be along the $\hat{x}$ direction, in which case the mirror symmetry $\mathcal{M}_x$ is reflection in the $y - z$ plane perpendicular to the superconducting layer. This acts on the non-BdG Hamiltonian as

$$\mathcal{M}_x^{-1} H(\mathbf{p}) \mathcal{M}_x = H(\bar{\mathbf{p}}) \tag{S39}$$

where $\bar{\mathbf{p}} = (-p_x, p_y)$. Since this reflection also reverses the y and z components of the spin, in the spin basis $\mathcal{M}_x$ acts as $i\sigma^x$, while in the SOC basis (S5) it is momentum dependent, $\mathcal{M}_x = -i\tau e^{-i\phi(\mathbf{p})}$.

This action of mirror symmetry can be extended to the BdG spinors, to give

$$\tilde{\mathcal{M}}_x(\mathbf{p}) = \begin{pmatrix} \mathcal{M}_x(\mathbf{p}) & 0 \\ 0 & -\mathcal{M}_x^\dagger(-\mathbf{p}) \end{pmatrix}$$
$$= \begin{pmatrix} e^{i\phi(\mathbf{p})} & 0 \\ 0 & -e^{-i\phi(-\mathbf{p})} \end{pmatrix} \tag{S40}$$

This acts on the BdG Hamiltonian according to:

$$\tilde{\mathcal{M}}_x^{-1} H_{\eta\tau}^{(BdG)}(\mathbf{p}) \tilde{\mathcal{M}}_x = H_{\eta\tau}^{(BdG)}(\bar{\mathbf{p}}) \tag{S41}$$

Here the relative sign between the two non-vanishing components of $\tilde{M}$ is determined by how the gap functions transform under the mirror symmetry. In the regime of interest, where the SC gap is odd under $p_x \to -p_x$, the appropriate choice is minus.

To understand the effects of symmetry, we follow the approach of Ref. [43]: specifically, we will show that in the low-energy theory obtained by linearizing the model near the nodes, there are no symmetry-allowed mass terms. To see this, we first linearize the Hamiltonian in the region $b > \alpha_R P_F$ around the pair of nodes at $p_x = 0$. This gives a 4×4 low-energy effective Hamiltonian, with a new index L, R to keep track of the two nodes. We define τ^μ to be the Pauli matrices acting on the L, R indices, while ς^μ are Pauli matrices acting on the 2 indices of the BdG spinors (i.e. on the particle-hole indices). The linearized Hamiltonian has the form

$$\mathcal{H} = \delta p_y \varsigma^z \otimes \tau^z + p_x \varsigma^x \otimes \tau^0 \tag{S42}$$

where $\delta p_y = p_y - p_y^{(\text{node})}$.

In this basis the particle-hole symmetry, which interchanges the two nodes, acts via $\mathcal{C} = \varsigma^x \otimes \tau^x \mathcal{K}$. Near the nodes, which lie on the mirror plane (i.e. at $p_x = 0$), the mirror symmetry has the form $\tilde{\mathcal{M}}_x(\mathbf{p}) = \varsigma^z$. Since the mirror symmetry acts in the same way on both nodes in that case, in our linearized theory mirror symmetry acts via

$$\tilde{\mathcal{M}}_x = \varsigma^z \otimes \tau^0 . \tag{S43}$$

Note that Eq. (S40) implies that the action of $\tilde{\mathcal{M}}_x$ on the mirror plane changes discontinuously at $b = \alpha_R p_F$; for $b < \alpha_R p_F$, $\tilde{\mathcal{M}}_x$ is proportional to the identity matrix (times τ^z, in terms of the 4×4 matrices relevant to our effective low-energy theory).

In order to show that the nodes for $b > \alpha_R p_F$ are protected, we now consider what happens when we add a generic symmetry-allowed term $h(\delta p_y, p_x) \varsigma^\mu \otimes \tau^\nu$ to the Hamiltonian. Note that we do not wish to allow terms that couple the two nodes, as these break translational symmetry; thus we require $\nu = 0$ or z. Recall that the symmetries are

$$\mathcal{C}^{-1} \mathcal{H}(\delta p_y, p_x) \mathcal{C} = -\mathcal{H}(-\delta p_y, -p_x)$$
$$\tilde{\mathcal{M}}_x^{-1} \mathcal{H}(\delta p_y, p_x) \tilde{\mathcal{M}}_x = \mathcal{H}(\delta p_y, -p_x) . \tag{S44}$$

Thus $h(-\delta p_y, -p_x) = \pm h(\delta p_y, p_x)$, where $\mathcal{C}^{-1} \varsigma^\mu \otimes \tau^\nu \mathcal{C} = \mp \varsigma^\mu \otimes \tau^\nu$. Similarly $h(\delta p_y, -p_x) = \pm h(\delta p_y, p_x)$, where $\tilde{\mathcal{M}}_x^{-1} \varsigma^\mu \otimes \tau^\nu \tilde{\mathcal{M}}_x = \pm \varsigma^\mu \otimes \tau^\nu$. To gap out the nodes we must have $h(0,0) \neq 0$; thus we need plus signs in both cases. Hence $\varsigma^\mu \otimes \tau^\nu$ anti-commutes with $\mu^x \otimes \tau^x \mathcal{K}$ and commutes with $\varsigma^z \otimes \tau^0$.

For $b > \alpha_R p_F$, to leading order in momenta about the nodes the only symmetry-allowed terms are $m\varsigma^0 \otimes \tau^z$ and $m\varsigma^z \otimes \tau^0$. The second term, which plays the role of a chemical potential shift at each node, does not lift the nodes; rather it shifts them in opposite directions along the y axis, from $p_y = \pm p_F$ to $p_y = \pm(p_F + m)$.

The $m\varsigma^0 \otimes \tau^z$ term, on the other hand, shifts the nodes in opposite directions in energy by an amount $|m|$. Taken

literally, this changes the nodes to small BdG Fermi surfaces at the Fermi energy. However, this is deceptive: in fact, the term $m\varsigma^0 \otimes \tau^z$ shifts the normal state FS, defined as the contour of zero normal state energy (given by the upper left element of both L and R blocks of $\mathcal{H}$) by m in the BZ. To see this, observe that at $p_x = 0$, the FS at both nodes is determined by $\delta p_y + m = 0$, and therefore must shift for non-zero m. Since pairing is between electrons *on* the FS, the Cooper pair in this case acquires a finite momentum m. As a result, the Nambu spinors should properly be redefined as $(c_{\mathbf{p}+m\hat{\mathbf{y}}}, c^\dagger_{-\mathbf{p}+m\hat{\mathbf{y}}})$. This transformation applied to (85) can be seen to amount precisely to adding $-m\varsigma^0 \otimes \tau^z$, thus canceling the offending term and bringing the nodes back to zero energy. After correctly accounting for this finite-momentum pairing, the edge modes remain flat in the ground state.

Tight Binding Model for Edge Mode Spectrum

To produce the plot in Fig. 4 we used a tight binding model defined on the triangular lattice, which we describe in more detail here. The Hamiltonian has the general form

$$H = H_0 + H_Z + H_{SC} \qquad (S45)$$

The first term describes the normal state band structure in the presence of SOC; the second-term is the Zeeman coupling due to in-plane magnetic field; and the last term represents the superconducting pairing gap. For simplicity we use a tight-binding model that only includes the $\eta = \Gamma$ pocket Fermi surface, since the $\pm K$ pockets are unimportant for the crystalline nodal topological superconductor.

We describe our model in terms of the creation operators $d^\dagger_{i,\alpha}$, where $\alpha = \uparrow, \downarrow$ is a spin index, and i is a site index. We have

$$H_0 = \sum_{i\alpha} \mu\, d^\dagger_{i\alpha} d_{i\alpha} + \sum_{\langle ij \rangle \alpha} t\, d^\dagger_{i\alpha} d_{j\alpha}$$
$$+ \sum_{\langle ij \rangle \alpha\beta} \left[4i\lambda\nu_{ij}\sigma^z_{\alpha\beta} + \frac{i\alpha_R}{3}\hat{\mathbf{z}} \cdot (\boldsymbol{\sigma} \times \mathbf{a}_{ij})_{\alpha\beta} \right] d^\dagger_{i\alpha} d_{j\beta}$$
$$H_Z = \sum_{i\alpha\beta} (\mathbf{b} \cdot \boldsymbol{\sigma})_{\alpha\beta}\, d^\dagger_{i\alpha} d_{i\beta} \qquad (S46)$$
$$H_{SC} = \frac{1}{2}\sum_{ij\alpha\beta} [\Delta]^{ij}_{\alpha\beta}\, d^\dagger_{i\alpha} d^\dagger_{j\beta} + \text{h.c.}$$

where $\mathbf{a}_{ij} \in \{\pm\mathbf{a}_1, \pm\mathbf{a}_2, \pm\mathbf{a}_3\}$ is the vector from site i to site j, and $\nu_{ij} = 1\ (-1)$ if the vector is $\mathbf{a}_1$, $-\mathbf{a}_2$, $\mathbf{a}_3$ ($-\mathbf{a}_1$, $\mathbf{a}_2$, $-\mathbf{a}_3$) . For our triangular lattice, $\mathbf{a}_1 = (a, 0)$ and $\mathbf{a}_2 = \frac{a}{2}(1, \sqrt{3})$, $\mathbf{a}_3 = \mathbf{a}_2 - \mathbf{a}_1 = \frac{a}{2}(-1, \sqrt{3})$. We consider the singlet-instability regime, in the crystalline nodal topological phase where $b \gg \alpha_R p_F$. In this region we can take

$$\Delta^{ij} = \Delta_0 \nu_{ij} (\sigma^x \cos\vartheta + \sigma^y \sin\vartheta) i\sigma^y \qquad (S47)$$

where ϑ is the direction of the magnetic field. The numerical coefficients are chosen to match the $\mathbf{k} \cdot \mathbf{p}$ Hamiltonian (including the value of p_F). The specific values used in the Figure are listed at the end of this section.

Our cylinder is created by taking periodic boundary conditions in the vertical y direction, and open zig-zag boundary conditions along the x direction. To produce the plot, we Fourier transform in the y direction:

$$d_{\mathbf{R_i}\alpha} = \frac{1}{\sqrt{N}} \sum_{p_y} d_{R_{ix}p_y\alpha} e^{-ip_y R_{iy}} \equiv \frac{1}{\sqrt{N}} \sum_{p_y} d_{ip_y\alpha} e^{-ip_y R_{iy}} \qquad (S48)$$

where $\mathbf{R}_i = (R_{ix}, R_{iy})$. Note that i labels the x coordinates of the sites which go in increments of $a/2$, while the period along the y axis is actually doubled since identical sites are now separated by $2\mathbf{a}_2$, resulting in the folding of the 1D Brillouin zone (which has a period of $\frac{2\pi}{\sqrt{3}a}$).

The resulting BdG Hamiltonian on the cylinder can be expressed

$$H_{BdG} = \frac{1}{2}\sum_{ij,p_y} \Psi^\dagger_{i,p_y} \mathcal{H}^{ij}(p_y) \Psi_{j,-p_y} \qquad (S49)$$

where $\Psi_{i,p_y} = \left(d_{i,p_y\uparrow}, d_{i,p_y\downarrow}, d^\dagger_{i,-p_y\uparrow}, d^\dagger_{i,-p_y\downarrow} \right)$ and

$$\mathcal{H}^{ij}(p_y) = \begin{pmatrix} \mathcal{H}^{ij}_{kin}(p_y) & \Delta^{ij}(p_y) \\ -\left(\Delta^{ij}(-p_y)\right)^* & -\left(\mathcal{H}^T_{kin}(-p_y)\right)^{ji} \end{pmatrix} \qquad (S50)$$

where we have defined

$$H_0 + H_Z = \sum_{ij\alpha\beta} (\mathcal{H}_{kin}(p_y))^{ij}_{\alpha\beta}\, d^\dagger_{ip_y\alpha} d_{jp_y\beta} \qquad (S51)$$

In the presence of both Rashba SOC and in-plane magnetic field, the Fermi surfaces are shifted in the direction perpendicular to the magnetic field, so the correct SC ground state has a finite center of mass momentum. To account for that, we need to shift $p_y \to \tilde{p}_y = p_y + P$ in the equations above. Since the shift is opposite on inner and outer FS's, P is an even function of p_y. The resulting Hamiltonian is

$$H = \frac{1}{2}\sum_{ij,p_y} \Psi^\dagger_{i,p_y+P(p_y)} \mathcal{H}^{ij}(p_y) \Psi_{j,-p_y+P(p_y)} \qquad (S52)$$

with

$$\mathcal{H}^{ij}(p_y) = \begin{pmatrix} \mathcal{H}^{ij}_{kin}(p_y + P(p_y)) & \Delta^{ij}(p_y) \\ -\left(\Delta^{ij}(-p_y)\right)^* & -\left(\mathcal{H}^T_{kin}(-p_y + P(p_y))\right)^{ji} \end{pmatrix} \qquad (S53)$$

where the gap has the same form as in Eq. (S47) , but the spinor Ψ is now given by:

$$\Psi^\dagger_{i,p_y} = \begin{pmatrix} d_{i,p_y+P(p_y),\uparrow} \\ d_{i,p_y+P(p_y),\downarrow} \\ d^\dagger_{i,-p_y+P(p_y),\uparrow} \\ d^\dagger_{i,-p_y+P(p_y),\downarrow} \end{pmatrix} . \qquad (S54)$$

The resulting spectrum is plotted in Fig. 4 with the number of sites along the non-periodic x direction $N = 200$ (which corresponds to 100 unit cells due to period doubling), $t = 1$, $\mu = 0$, $b = 1$, $\lambda = 0.2$, $\alpha_R = 0.1$, and $\vartheta = 0$ corresponding to the $\Gamma - K$ direction in the Brillouin zone for which a pair of nodes appears. To account for the shifts in that case we take $P(p_y) = 0.07 + 0.025 \cos \sqrt{3} p_y$. Note that $\tilde{p}(p_y) = p_y + P(p_y)$ is a monotonic function of p_y in that case.